ARTICLE   OPEN

Check for updates

Quantum dynamics of topological strings in a frustrated Ising antiferromagnet

Zheng Zhou [1,2], Changle Liu[3,4], Zheng Yan [5,6✉], Yan Chen[1,7✉] and Xue-Feng Zhang[3,8✉]

We investigate the quantum dynamics of the antiferromagnetic transverse field Ising model on the triangular lattice through large-scale quantum Monte Carlo simulations and stochastic analytic continuation. This model effectively describes a series of triangular rare-earth compounds, for example, TmMgGaO$_4$. At weak transverse field, we capture the excitations related to topological quantum strings, which exhibit continuum features described by XY chain along the strings and those in accord with 'Luttinger string liquid' in the perpendicular direction. The continuum features can be well understood from the perspective of topological strings. Furthermore, we identify the contribution of strings from the excitation spectrum. Our study provides characteristic features for the experimental search for string-related excitations and proposes a theoretical method to pinpoint topological excitations in the experimental spectra.

INTRODUCTION

Frustrated magnets provide an ideal playground for exotic emergent phenomena[1,2]. In many cases, gauge structures can emerge due to local constraints imposed by competing interactions, giving rise to exotic states of matter like quantum spin liquid with fractionalised excitations and long-range entanglement[3-9]. Excitations violating such local constraints are frequently referred to as spinons, which are the gauge charges in the emergent gauge theory[10-12]. Spinons are point-like topological defects since a single spinon cannot be created/annihilated locally and such processes must be involved in pairs. Meanwhile, gauge theories also support string-like excitations, which connect a pair of spinons with opposite charges and mediate the effective interaction between them. While the spinon pair is annihilated along a non-contractible closed trajectory, such string becomes topological in nature, which we dub as 'topological string'[13,14].

In contrast to spinon excitations that are typically located at higher energies, quantum strings are basic degrees of freedom participating in low-energy physics. Their dynamics reflects the fluctuations of the background gauge field[15,16]. Quantum strings are 1d objects in space that can be described as two-dimensional worldsheets in spacetime[17]. As emergent topological defects with finite dimensions, strings have much more internal degrees of freedom (corresponding to their vibration) and are thus expected to bring much richer physics. Strings appear in broad contexts in condensed matter physics, such as in high-temperature superconductors[18-22], quantum spin ice[23-25] and incommensurability[18,26,27]. They can even be directly observed via the ultra-cold atoms in the optical lattice[28,29]. However, in contrast to well-studied point-like excitations, strings are paid much less attention.

The quest for exploring string dynamics is also motivated by the rapid progress on frustrated rare-earth materials. Recently, a number of rare-earth pyrochlore, Kagomé and triangular lattice magnets have been evidenced to be described by frustrated quantum Ising models[30-35] which exhibit emergent gauge structures. For the triangular lattice, a large class of materials are described by the transverse field Ising model (TFIM)[31,34], a typical model that can be understood from the perspective of topological strings[15,16,29]: String picture can be utilised to understand its phase diagram[15,16] as well as to depict the quantum fluctuations therein[36-39]. Among these materials, a typical one is TmMgGaO$_4$ (TMGO). The spin excitation spectra was recently discovered in the neutron scattering experiment[31], and the so-called 'roton' excitation was claimed to relate to the BKT physics[33,40,41]. However, direct signatures of string excitations are absent from the neutron spectrum.

In this manuscript, we study a generic antiferromagnetic TFIM on the triangular lattice relevant to triangular lattice rare-earth compounds. Through large-scale quantum Monte Carlo (QMC) simulations[42], we focus on the dynamical signatures of quantum string excitations. At weak transverse field, we find continuum excitations at low energies that accords with the internal vibration and mutual interactions of quantum strings. In particular, the internal vibration matches well with the continuous spectrum of spin-1/2 XY chain, while the string interactions induce excitations exhibiting features of Luttinger liquid[43]. It should be noted that these continuum spectroscopic properties go beyond the effective field theory, where for the latter only coherent spin waves were predicted at low energies. Our work provides insight into understanding the dynamical properties of triangular quantum Ising antiferromagnet such as TMGO.

RESULTS

Starting from rare-earth compounds

We begin with the nearest-neighbour spin-1/2 TFIM relevant to triangular rare-earth compounds

$$H = J \sum_{\langle ij \rangle} S_i^z S_j^z - \Delta \sum_i S_i^x \qquad (1)$$

[1]Department of Physics and State Key Laboratory of Surface Physics, Fudan University, Shanghai 200438, China. [2]Perimeter Institute for Theoretical Physics, Waterloo, ON N2L 2Y5, Canada. [3]Department of Physics, and Center of Quantum Materials and Devices, Chongqing University, Chongqing 401331, China. [4]Shenzhen Institute for Quantum Science and Technology and Department of Physics, Southern University of Science and Technology, Shenzhen 518055, China. [5]Beihang Hangzhou Innovation Institute, Yuhang, Hangzhou 310023, China. [6]Department of Physics and HKU-UCAS Joint Institute of Theoretical and Computational Physics, The University of Hong Kong, Pokfulam Road, Hong Kong SAR, China. [7]Collaborative Innovation Center of Advanced Microstructures, Nanjing 210093, China. [8]Chongqing Key Laboratory for Strongly Coupled Physics, Chongqing University, Chongqing 401331, China. ✉email: zhengyan@hku.hk; yanchen99@fudan.edu.cn; zhangxf@cqu.edu.cn

Here S is the effective spin-1/2 moment acting on the lowest two crystal field levels of the non-Kramers ion. J denotes the nearest neighbour antiferromagnet coupling and the Δ is the energy splitting between the lowest crystal-field levels. The origin of the crystal field splitting term Δ depends on the nature of crystal field levels. For non-Kramers doublet systems, the crystal field degeneracy is protected by the C_3 on-site point group symmetry, therefore Δ is induced by breaking such symmetry, e.g., by applying in-plane uniaxial pressure. For TMGO and some other Tm-based materials, the lowest two crystal field levels form a nondegenerate dipole-multipole doublet. The lowest crystal fields exhibit intrinsic splitting Δ since they carry the singlet representation of the point group. To quantitatively compare with the TMGO experiment, we also introduce a next-nearest-neighbour interaction $H_{J'} = J' \sum_{\langle\langle ij \rangle\rangle} S_i^z S_j^z$ perturbation term to the Hamiltonian[34]. The effective model is illustrated in Fig. 2c inset.

The best-fit parameters for TMGO were found in the former work[33] to be $J = 0.99$ meV, $j' = 0.05$ meV and $\Delta = 0.54$ meV. Hereafter we set the NN coupling as the energy unit $J = 1$. We carry out a QMC simulation[42,44,45] combined with SAC technique[46–48] to measure the spin excitation spectrum. The simulation is performed on $L \times L$ lattice ($L = 24$) with periodic boundary conditions. The temperature is set $T = 1/4L = 1/96$ to mimic the ground state result. In inelastic neutron scattering experiments, what is measured is the dynamical S^z-S^z correlator given by

$$S^{zz}(\mathbf{q}, \omega) = \frac{1}{2\pi L^2} \sum_{ij} \int_{-\infty}^{+\infty} dt\, e^{i\mathbf{q}\cdot(\mathbf{r}_i - \mathbf{r}_j) - i\omega t} \langle S_i^z(0) S_j^z(t) \rangle \tag{2}$$

Our measured excitation spectrum is presented in Fig. 1a.

At the parameters for TMGO, the simulated result agrees well with the previous inelastic neutron scattering experiment[31] and the previous QMC work[33] (See Supplementary Fig. 1). Notice that for TMGO, Δ is large where the system has been close to the clock-paramagnetic transition point (Fig. 2f). To gain a better understanding of the physics deep in the clock phase, we also measure the excitation spectra with decreased Δ. We find that with decreasing Δ, the spectrum splits into two branches. The higher-lying and lower-lying branches lie at the energy scale of J and Δ, respectively, see Fig. 1b, c.

The string description

To better understand the two branches of excitations, we first consider the classical Ising limit $\Delta = 0$. In this case, the ground state is macroscopically degenerate, consisting all the configurations that satisfy the '2-up-1-down' or '1-up-2-down' triangle-rule within each elementary triangle. Such local constraints give rise to emergent $U(1)$ gauge structures at low energies which further lead to emergent topological strings and topological sectors. Instead of understanding strings from dimers and gauge theories, here we present a more intuitive way from an alternative domain wall perspective[49–51]. We choose the stripe state (Fig. 2d) as the reference configuration. The reason we choose the stripe state as the reference state is that any local operation acting upon this state violates the local constraint, hence there are no low-energy excitations within the stripe bulk. With this setup, all spin configurations which obey the triangle-rule can be expressed as domains of stripe state, where domain walls form closed directed strings (Fig. 2a, strings 1–3). In other words, one selects out the bonds in x-direction connecting anti-parallel spins, and connects their mid-points into strings. The strings can be visualised in measurements (See Supplementary Fig. 4). Under periodic boundary conditions, strings wrapping around non-contractible loops cannot be created or annihilated within finite steps of operation, which strongly reflects its topological feature in nature. Therefore the number of topological strings N_s can be used to label different topological sectors. On the other hand, breaking of
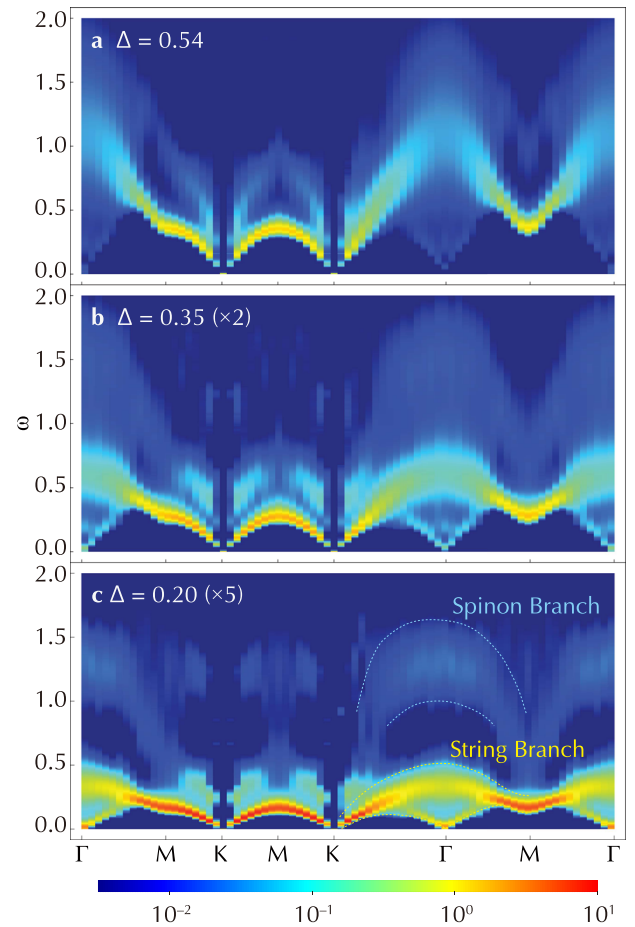

Fig. 1 The spectra at different transverse field Δ. a The parameter $\Delta = 0.54$ and $J' = 0.05$ corresponds to the material TMGO. **b** $\Delta = 0.35$, $J' = 0.35$ and (**c**) $\Delta = 0.20$, $J' = 0.020$ are for lower energy splitting. The circled areas in (**c**) demonstrate the splitting of two branches. The path taken in the Brillouin zone is specified in the inset of (**a**). The spectra are plotted in logarithmic scale to accommodate more details. For the plots in linear scale, see Supplementary Fig. 2.

triangle-rule corresponds to spinon excitations at the energy scale of J[15,16] (Fig. 2a, string 4). This is related to the high energy excitations.

Once the transverse field Δ is turned on, quantum dynamics are present. When $\Delta \ll J$, the low energy excitations do not mix up with the spinon excitations at a higher energy level. As shown above, the low energy quantum excitations are completely provided by the quantum strings. Here we first consider the excitations where only one string is involved, i.e., the internal vibration of a single string. The shape of a string is specified by its segments $\{\mathbf{s}_1, \ldots, \mathbf{s}_{L_y}\}$, which take on the values $\mathbf{r}$ and $\mathbf{l}$ (shown in Fig. 2a). Upon the action of the transverse field, a pair of antiparallel nearest-neighbour spins are flipped, i.e., $|\ldots \mathbf{rl}\ldots\rangle \leftrightarrow |\ldots \mathbf{lr}\ldots\rangle$ (Fig. 2b). According to the first-order perturbation theory, these fluctuations can be mapped onto a spin-1/2 XY chain, with spin values $\tau^z = \pm 1/2$ represents $\mathbf{r}$ and $\mathbf{l}$ segments

$$H_{\text{eff}} = -\frac{\Delta}{2} \sum_{i=1}^{L_y} \left(\tau_i^+ \tau_{i+1}^- + \tau_i^- \tau_{i+1}^+ \right) \tag{3}$$

The effective model is exactly solvable under Jordan-Wigner transformation. Therefore, one can predict a continuous spectrum due to effective Jordan-Wigner fermions excitations corresponding
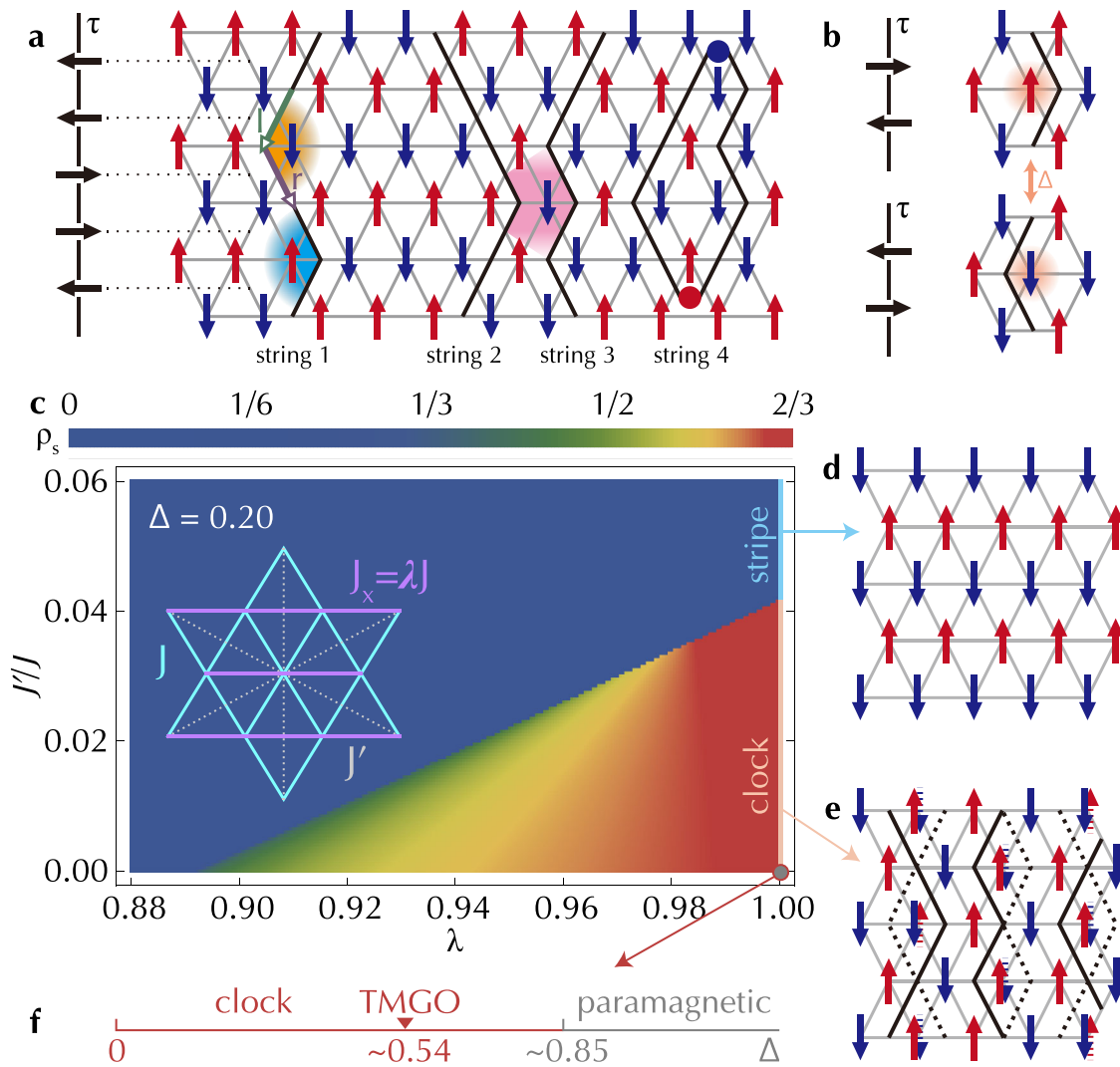
Fig. 2 An illustration of the emergent strings in frustrated TFIM. a An example of string mapping of a spin configuration. Strings 1, 2 and 3 don't involve triangle-rule-breaking configurations and are thus directional. The **l** and **r** vectors on string 1 denote the two directions of the segments. The spin chain labelled τ on the left illustrates the effective spin-1/2 configuration mapped from string 1. The orange and cyan shaded angles on string 1 denote a kink-antikink pair. The pink shaded area illustrates that two nearby strings induce repulsion. String 4 is a closed non-topological string connecting two spinons denoted by red and blue points. **b** The elementary flipping process brought by the transverse field $|lr\rangle \leftrightarrow |rl\rangle$. The transverse field acts upon the shaded spin. **c** The ground state string density as a function of anisotropy λ and NNN coupling J', obtained from large scale QMC simulation. Inset: an illustration of the lattice setup. **d**, **e** Configuration and string correspondence of two specific phases: stripe phase (**d**) with average string density $\langle \rho_s \rangle = 0$ and clock phase (**e**) with $\langle \rho_s \rangle = 2/3$. The collapsed arrows denote the superposition of spin-up and down. Correspondingly, the strings are superpositions of configurations denoted by the solid and dashed lines. **f** The phase diagram at $\lambda = 1$ and $J' = 0$, at different transverse field Δ.

to kink-antikink pairs in the language of strings. This vibration also brings an energy favour $E_k = -\Delta L_y/\pi$ to each string, stablizing it energetically against perturbations.

When multiple strings are considered, their interaction becomes significant to the quantum excitations. The non-crossing condition first imposes a hard-core repulsion on strings. The vibration of strings then turns this hard-core repulsion into a dynamic one[49]. Specifically, when two strings come close to each other (e.g., the string 2 and 3 in Fig. 2a), their vibration will be constrained, reducing the energy gain from internal vibration (See Supplementary Note 1). This loss of vibration energy can be equivalently regarded as the repulsion interaction between them. As former work[27] has identified, the dynamic repulsion can be described by a power-law long-range potential. In other words, the internal vibration of strings can also generate mutual dynamic interaction among them.

Dilute string limit

The vibration inside the strings, together with the repulsion interaction between them, determines the low energy excitations of TFIM. To study these two kinds of excitations separately, we turn to the dilute string limit where the strings are far apart and the interaction between them is weak, so that the internal string vibration is not affected by string interaction. This can be parametrised by a quantity called the string density $\rho_s = N_s/L_x$. The string density is determined by measuring the nearest-neighbor correlation $\langle \rho_s \rangle = \frac{1}{2}\left(1 - 4\langle S_r^z S_{r+\hat{x}}^z \rangle\right)$. In particular, the stripe phase and clock phase, whose configurations and string correspondence are depicted in Fig. 2d, e, have averaged string density $\langle \rho_s \rangle_{stripe} = 0$ and $\langle \rho_s \rangle_{clock} = 2/3$. The string density can be tuned through introducing various perturbations, like the nearest-neighbour exchange anisotropy $H_\lambda = (\lambda - 1)J \sum_{\langle ij \rangle_x} S_i^z S_j^z$[27]. Here $\langle ij \rangle_x$ denote the NN bonds in x-direction (Fig. 2c inset). The string
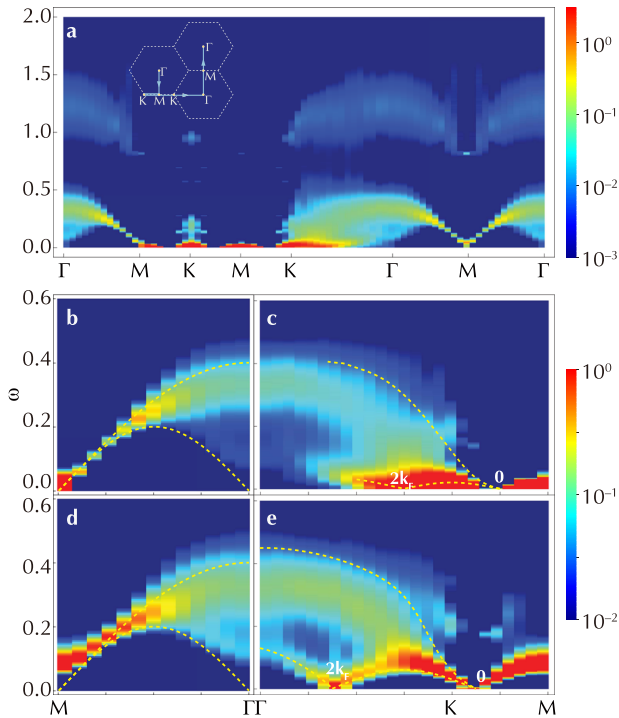
Fig. 3 The spectra at low string density. a The spectra at string density $\rho_s = 1/3$ measured at $\lambda = 0.895$, $\Delta = 0.2$, system size $L = 24$ and temperature $T = 1/96$ in the unit of J. The path taken in the Brillouin zone is specified in the inset. **b, c** The zoom-in of low energy region are dived into parallel to the strings (**b**) along ΓM line and perpendicular to the strings (**c**) along ΓKM line respectively. **d, e** The low energy excitation spectra measured at $\lambda = 0.91$ and $\rho_s = 1/2$ includes parallel to the strings (**d**) along ΓM line and perpendicular to the strings (**e**) along ΓKM line respectively. The dashed lines denote the anticipated results in spin-1/2 XY chain (**b, d**) and Luttinger liquid (**c, e**). The gray italic momentum labels '0' and '$2k_F$' are the momenta measured from the Fermi point of the projected 1d system.

density $\rho_s(\lambda, J')$ as a function of exchange anisotropy λ and NNN interaction J' are measured through a Monte Carlo simulation, shown in Fig. 2c (See Supplementary Note 2). By increasing J', the system enters the stripe phase from the clock phase through a first-order transition; by decreasing λ, the string density ρ_s decreases from 2/3 to 0 continuously.

We take $J' = 0$ and tune $0 < \lambda < 1$ to fine-tune the string density to a comparatively low lever $\langle \rho_s \rangle = 1/3$ and 1/2. The energy hierarchy in the spectrum persists (Fig. 3a). The spinon branch and the string branch stay at the energy scale of J and Δ, respectively. To look more carefully into the string excitations, we scrutinise the low energy spectrum along ΓM and ΓKM lines (Fig. 3b–e).

The spectrum along the ΓM line corresponds to the internal string vibration. In the case of nearly independent strings at $\rho_s = 1/3$ (Fig. 3b), the spectrum is continuous and enveloped by two dome-like curves, most extensive at Γ point and shrinking when moving towards M point. We find these features in good agreement quantitatively with the continuous spectrum of spin-1/2 XY chain (Fig. 3b, grey dashed lines) (See Supplementary Note 5), where Γ and M points correspond to $k = \pi$ and 0 momenta of the effective XY chain, respectively. On the other hand, when increasing the string density, the effective repulsion affects the internal vibration of strings, rendering the excitation gapped (Fig. 3d).

The spectrum along the ΓKM line corresponds to the dynamics that come from string interaction. The spectrum exhibits continuous features. Two nearly gapless points locate at

$k_x = \pi(2 - \langle \rho_s \rangle)$ and $\pi(2 - 3\langle \rho_s \rangle)$ (Fig. 3c, e). Whether these points are truly gapless depends on the commensuracy of the string density. At commensurate string density (such as $\langle \rho_s \rangle = 2/3$ in clock phase), the high order scattering process will open a gap in the excitation. However, such gap lies at a much lower energy level than our string description. The dispersions in the vicinity of the nearly gapless points are linear. These features hint at the spectroscopic similarity to Luttinger liquid[43] (See Supplementary Note 3). In fact, projecting onto the perpendicular direction, the strings can be described with spinless fermions with long-range repulsion moving in 1 d. The two nearly gapless points correspond to the momentum points 0 and $2k_F$ measured from the Fermi point, with the Fermi momentum of the strings $k_F = \pi\langle \rho_s \rangle$, in accordance with the spectroscopic features of 'Luttinger string liquid' (Fig. 3c, e, dashed lines).

String and spinon spectra

Having figured out the relation between different string-related excitations and their features in the spectrum, we now return to the isotropic case (i.e., the exchange anisotropy is tuned to $\lambda = 1$). To locate the excitations of different topological defects in the spectrum, we try to isolate the contributions from string and spinon excitations. We define a kink operator, which singles out the flippable spins at the kinks of the strings (See Supplementary Note 4), and a spinon operator, which singles out the spins on triangles with the same spin polarization. As the kink operator is only sensitive to string excitations, and the spinon operator only to spinon excitations, their dynamic correlations isolate the contribution of two respective excitations – At low field $\Delta = 0.2$ (Fig. 4a, d), the string spectrum has only low energy part and the spinon spectrum have only high energy part; while for higher Δ (Fig. 4c, f), the energy scales of two excitations nearly coincide, and they mix up into what we see in the spin spectrum measured by neutron scattering.

DISCUSSION

Our work focuses on the dynamical signature of quantum string excitations. We simulate the spectrum of frustrated TFIM on the triangular lattice, which is relevant to a large class of rare-earth magnets including the recently discovered TMGO. At low transverse field, we find continuum excitations at low energies. We show that the features of this continuum are in good agreement with the internal vibration and mutual interactions of quantum strings. In particular, the internal vibration (spectrum along ΓM line) matches well with the continuous spectrum of spin-1/2 XY chain, and the string interaction (spectrum along ΓKM line) induces excitations which exhibit the features of Luttinger liquid. Several trials can be considered in the experiment to observe the string-related excitations in the excitation spectra. If we can find materials with appropriate Δ/J, we expect well separation of string-related excitations from spinons in excitation spectrum[31,33,52,53]. In experiments, we can also study anisotropic models by applying in-plane uniaxial pressure. On the one hand, for non-Kramers doublet systems, the crystal field splitting Δ is generated and can be tuned by the applied pressure. This enables discovering string related excitations with appropriate Δ. On the other hand, the applied pressure also produces exchange anisotropy λ, which tunes the string density ρ_s. With sufficiently large λ one would access the dilute string region where the intra-string excitations may be observed. Besides rare-earth magnets, similar phenomena are also expected in other systems such as antiferroelectric materials[54], cold atoms[55] and quantum computer[56].

Our work not only provides insight into understanding the dynamical properties of triangular quantum Ising antiferromagnet such as TMGO, but also provides iconic features in the
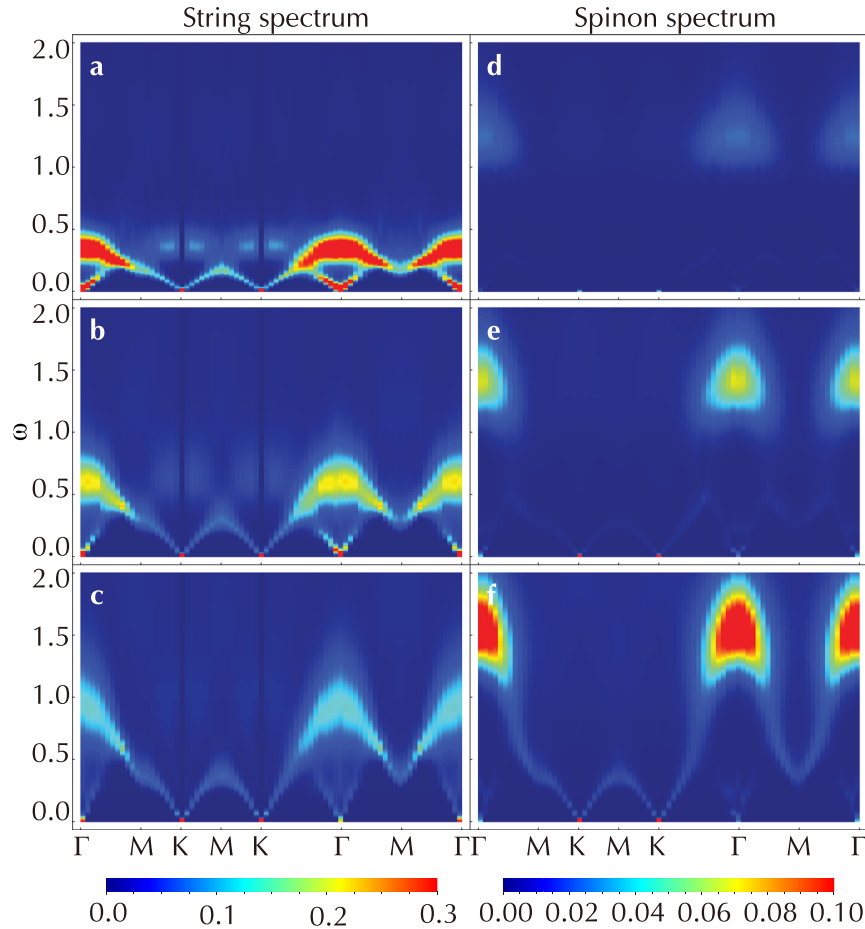
Fig. 4 The separated spectra of string excitations and spinon excitations. String spectra (**a**–**c**) and spinon spectra (**d**–**f**) with $L = 24$ and $T = 1/96$ at $\Delta = 0.20$, $J' = 0.020$ (**a, d**), $\Delta = 0.35$, $J' = 0.035$ (**b, e**) and $\Delta = 0.050$, $J' = 0.050$ (**c, f**).

spectrum for the experimental search for emergent strings, as well as deepening the understanding of emergent quantum strings in general.

METHODS

Stochastic series expansion (SSE)

We use SSE algorithm for the quantum Monte Carlo simulation of the transverse field Ising model[42,44,45]. In SSE, the evaluation of partition function Z is done by a Taylor expansion, and the trace is taken by summing over a complete set of suitably chosen basis.

$$Z = \sum_a \sum_{n=0}^\infty \frac{\beta^n}{n!} \langle a | (-H)^n | a \rangle \tag{4}$$

By writing the Hamiltonian as the sum of a set of operators whose matrix elements are easy to calculate $H = -\sum_i H_i$ and truncating the Taylor expansion at a sufficiently large cutoff M, we can further obtain

$$Z = \sum_a \sum_{\{i_p\}} \beta^n \frac{(M-n)!}{M!} \left\langle a \left| \prod_{p=1}^n H_{i_p} \right| a \right\rangle \tag{5}$$

To carry out the summation, a Markov chain Monte Carlo procedure can be used to sample the operator sequence $\{i_p\}$ and the trial state a. Diagonal update, where diagonal operators are inserted into and removed from the operator sequence, and cluster update, where diagonal and off-diagonal operates convert into each other, are adopted in the update strategy. For more details, see Supplementary Method 1.

Stochastic analytical continuation (SAC)

We adopted the SAC method to obtain the spectral function $S(\omega)$ from the imaginary time correlation $G(\tau)$ measured from QMC[46–48]. The spectral function $S(\omega)$ is connected to the imaginary time Green's function $G(\tau)$ through an integral $G(\tau) = \int_{-\infty}^{\infty} d\omega S(\omega) K(\tau, \omega)$ where $K(\tau,\omega)$ is the kernal function. For spin systems, $K(\tau, \omega) = (e^{-\tau\omega} + e^{-(\beta-\tau)\omega})/\pi$. To ensure the normalization of spectral function, we further modify the transformation,

$$G(\tau) = \int_0^\infty \frac{d\omega}{\pi} \frac{e^{-\tau\omega} + e^{-(\beta-\tau)\omega}}{1 + e^{-\beta\omega}} B(\omega) \tag{6}$$

where $B(\omega) = S(\omega)(1 + e^{-\beta\omega})$ is the renormalised spectral function.

In practice, $G(\tau)$ for a set of imaginary time $\tau_i(i = 1, \ldots N_\tau)$ is measured in QMC simulation together with the statistical errors. The renormalised spectral function is parametrised into large number of δ-functions $B(\omega) = \sum_{i=0}^{N_\omega} a_i \delta(\omega - \omega_i)$ whose positions are sampled. Then the fitted Green's functions $\tilde{G}_i$ from Eq. (6) and the measured Greens functions $\overline{G}_i$ are compared by the fitting goodness $\chi^2 = \sum_{i,j=1}^{N_\tau} (\tilde{G}_i - \overline{G}_i)(C^{-1})_{ij}(\tilde{G}_j - \overline{G}_j)$ where C_{ij} is the covariance matrix. A Metropolis process is utilised to update the series in sampling. The weight for a given spectrum is taken to follow a Boltzmann distribution $W(\{a_i, \omega_i\}) \sim \exp(-\chi^2/2\Theta)$ with Θ a virtue temperature. All the sampled spectral functions are then averaged to obtain the final result. For more details, see the Supplementary Method 2. As an evidence of the validity of SAC, we also compare the spectral function obtained from SAC with the lowest excitation frequency extracted directly from the imaginary time correlations (see the Supplementary Fig. 3).

DATA AVAILABILITY

The data that support the findings of this study are available from the authors upon reasonable request.

CODE AVAILABILITY
The computer codes that support the findings of this study are available from the authors upon reasonable request.

REFERENCES
1. Moessner, R. & Ramirez, A. P. Geometrical frustration. *Phys. Today* **59**, 24–29 (2006).
2. Vojta, M. Frustration and quantum criticality. *Rep. Prog. Phys.* **81**, 064501 (2018).
3. Read, N. & Sachdev, S. Large-N expansion for frustrated quantum antiferromagnets. *Phys. Rev. Lett.* **66**, 1773–1776 (1991).
4. Isakov, S. V., Gregor, K., Moessner, R. & Sondhi, S. L. Dipolar spin correlations in classical pyrochlore magnets. *Phys. Rev. Lett.* **93**, 167204 (2004).
5. Kitaev, A. Anyons in an exactly solved model and beyond. *Ann. Phys. (N. Y.).* **321**, 2–111 (2006).
6. Balents, L. Spin liquids in frustrated magnets. *Nature* **464**, 199–208 (2010).
7. Yan, Z., Wang, Y.-C., Ma, N., Qi, Y. & Meng, Z. Y. Topological phase transition and single/multi anyon dynamics of $\mathbb{Z}_2$ spin liquid. *npj Quant. Mater.* **6**, 39 (2021).
8. Yan, Z., Samajdar, R., Wang, Y.-C., Sachdev, S. & Meng, Z. Y. Triangular lattice quantum dimer model with variable dimer density. Preprint at https://arxiv.org/abs/2202.11100 (2022).
9. Yan, Z. Improved sweeping cluster algorithm for quantum dimer model. Preprint at https://arxiv.org/abs/2011.08457 (2020).
10. Castelnovo, C., Moessner, R. & Sondhi, S. Magnetic monopoles in spin ice. *Nature.* **451**. 42–45 (2008).
11. Chen, G. Dirac's "magnetic monopoles" in pyrochlore ice $U(1)$ spin liquids: Spectrum and classification. *Phys. Rev. B.* **96**, 195127 (2017).
12. Zhou, Z., Yan, Z., Liu, C., Chen, Y. & Zhang, X.-F. Emergent rokhsar-kivelson point in realistic quantum ising models. Preprint at https://arxiv.org/abs/2106.05518 (2021).
13. Fulde, P. & Pollmann, F. Strings in strongly correlated electron systems. *Ann. Phys. (Berl.).* **17**, 441–449 (2008).
14. Yan, Z., Zhou, Z., Wang, Y.-C., Meng, Z. Y. & Zhang, X.-F. Targeting topological optimization problem: Sweeping quantum annealing. Preprint at https://arxiv.org/abs/2105.07134 (2022).
15. Jiang, Y. & Emig, T. String picture for a model of frustrated quantum magnets and dimers. *Phys. Rev. Lett.* **94**, 110604 (2005).
16. Jiang, Y. & Emig, T. Ordering of geometrically frustrated classical and quantum triangular Ising magnets. *Phys. Rev. B.* **73**, 104452 (2006).
17. Iqbal, N. & McGreevy, J. Toward a 3d Ising model with a weakly-coupled string theory dual. *SciPost Phys.* **9**, 19 (2020).
18. Zaanen, J. & Gunnarsson, O. Charged magnetic domain lines and the magnetism of high-T_c oxides. *Phys. Rev. B.* **40**. 7391–7394 (1989).
19. Eskes, H., Grimberg, R., van Saarloos, W. & Zaanen, J. Quantizing charged magnetic domain walls: Strings on a lattice. *Phys. Rev. B.* **54**, R724–R727 (1996).
20. Machida, K. Magnetism in La_2CuO_4 based compounds. *Phys. C.* **158**, 192–196 (1989).
21. Zaanen, J. Order out of disorder in a gas of elastic quantum strings in $2+1$ dimensions. *Phys. Rev. Lett.* **84**, 753–756 (2000).
22. Zaanen, J., Osman, O. Y., Kruis, H. V., Nussinov, Z. & Tworzydlo, J. The geometric order of stripes and Luttinger liquids. *Philos. Mag. B.* **81**, 1485–1531 (2001).
23. Gingras, M. J. P. & McClarty, P. A. Quantum spin ice: a search for gapless quantum spin liquids in pyrochlore magnets. *Rep. Prog. Phys.* **77**, 056501 (2014).
24. Pomaranski, D. et al. Absence of Pauling's residual entropy in thermally equilibrated $Dy_2Ti_2O_7$. *Nat. Phys.* **9**, 353–356 (2013).
25. Morris, D. J. P. et al. Dirac strings and magnetic monopoles in the spin ice $Dy_2Ti_2O_7$. *Science* **326**, 411–414 (2009).
26. Birgeneau, J. R., Stock, C., Tranquada, M. J. & Yamada, K. Magnetic neutron scattering in hole-doped cuprate superconductors. *J. Phys. Soc. Jpn.* **75**, 111003 (2006).
27. Zhang, X.-F., Hu, S., Pelster, A. & Eggert, S. Quantum domain walls induce incommensurate supersolid phase on the anisotropic triangular lattice. *Phys. Rev. Lett.* **117**, 193201 (2016).
28. Mazurenko, A. et al. A cold-atom Fermi–Hubbard antiferromagnet. *Nature* **545**, 462–466 (2017).
29. Chiu, C. S. et al. String patterns in the doped Hubbard model. *Science* **365**, 251–256 (2019).
30. Dun, Z. et al. Quantum versus classical spin fragmentation in dipolar kagome ice $Ho_3Mg_2Sb_3O_{14}$. *Phys. Rev. X.* **10**, 031069 (2020).
31. Shen, Y. et al. Intertwined dipolar and multipolar order in the triangular-lattice magnet TmMgGaO4. *Nat. Commun.* **10**, 4530 (2019).
32. Li, Y. et al. Partial up-up-down order with the continuously distributed order parameter in the triangular antiferromagnet TmMgGaO4. *Phys. Rev. X.* **10**, 011007 (2020).
33. Li, H. et al. Kosterlitz-Thouless melting of magnetic order in the triangular quantum Ising material TmMgGaO4. *Nat. Commun.* **11**, 1111 (2020).
34. Liu, C., Huang, C.-J. & Chen, G. Intrinsic quantum Ising model on a triangular lattice magnet TmMgGao4. *Phys. Rev. Res.* **2**, 043013 (2020).
35. Chen, G. Intrinsic transverse field in frustrated quantum Ising magnets: Physical origin and quantum effects. *Phys. Rev. Res.* **1**, 033141 (2019).
36. Schlittler, T., Barthel, T., Misguich, G., Vidal, J. & Mosseri, R. Phase diagram of an extended quantum dimer model on the hexagonal lattice. *Phys. Rev. Lett.* **115**, 217202 (2015).
37. Orland, P. Exact solution of a quantum model of resonating valence bonds on the hexagonal lattice. *Phys. Rev. B.* **47**, 11280–11290 (1993).
38. Orland, P. Fermionic strings and the exact solution of edge models in three dimensions. *Int. J. Mod. Phys. B.* **05**, 2401–2438 (1991).
39. Orland, P. Exact solution of a quantum gauge magnet in $2 + 1$ dimensions. *Nucl. Phys. B.* **372**, 635–653 (1992).
40. Isakov, S. V. & Moessner, R. Interplay of quantum and thermal fluctuations in a frustrated magnet. *Phys. Rev. B.* **68**, 104409 (2003).
41. Lin, S.-Z., Kamiya, Y., Chern, G.-W. & Batista, C. D. Stiffness from disorder in triangular-lattice Ising thin films. *Phys. Rev. Lett.* **112**, 155702 (2014).
42. Sandvik, A. W. Finite-size scaling of the ground-state parameters of the two-dimensional Heisenberg model. *Phys. Rev. B.* **56**, 11678–11690 (1997).
43. Haldane, F. D. M. 'Luttinger liquid theory' of one-dimensional quantum fluids. I. properties of the Luttinger model and their extension to the general 1d interacting spinless Fermi gas. *J. Phys. C.* **14**, 2585–2609 (1981).
44. Sandvik, A. W. Stochastic series expansion method for quantum Ising models with arbitrary interactions. *Phys. Rev. E.* **68**, 056701 (2003).
45. Avella, A. & Mancini, F. *Strongly correlated systems: numerical methods*, vol. 176 (Springer, Berlin. 2013).
46. Sandvik, A. W. Stochastic method for analytic continuation of quantum Monte Carlo data. *Phys. Rev. B.* **57**, 10287–10290 (1998).
47. Shao, H. et al. Nearly deconfined spinon excitations in the square-lattice spin-1/2 Heisenberg antiferromagnet. *Phys. Rev. X.* **7**, 041072 (2017).
48. Sandvik, A. W. Constrained sampling method for analytic continuation. *Phys. Rev. E.* **94**, 063308 (2016).
49. Zhang, X.-F. & Eggert, S. Chiral edge states and fractional charge separation in a system of interacting bosons on a kagome lattice. *Phys. Rev. Lett.* **111**, 147201 (2013).
50. Wan, Y. & Tchernyshyov, O. Quantum strings in quantum spin ice. *Phys. Rev. Lett.* **108**, 247210 (2012).
51. Wan, Y., Carrasquilla, J. & Melko, R. G. Spinon walk in quantum spin ice. *Phys. Rev. Lett.* **116**, 167202 (2016).
52. Shen, Y. et al. Evidence for a spinon Fermi surface in a triangular-lattice quantum-spin-liquid candidate. *Nature* **540**, 559–562 (2016).
53. Da Liao, Y. et al. Phase diagram of the quantum ising model on a triangular lattice under external field. *Phys. Rev. B.* **103**, 104416 (2021).
54. Shen, S.-P. et al. Quantum electric-dipole liquid on a triangular lattice. *Nat. Commun.* **7**, 10569 (2016).
55. Britton, J. W. et al. Engineered two-dimensional Ising interactions in a trapped-ion quantum simulator with hundreds of spins. *Nature* **484**, 489–492 (2012).
56. King, A. D. et al. Observation of topological phenomena in a programmable lattice of 1,800 qubits. *Nature* **560**, 456–460 (2018).

AUTHOR CONTRIBUTIONS

X.-F.Z., Z.Z. and Z.Y. initiated the work. Z.Z. and Z.Y. performed the Monte Carlo simulations. All authors contributed to the analysis of the results. X.-F.Z. and Y.C. supervised the project.

COMPETING INTERESTS

The authors declare no competing interests.

ADDITIONAL INFORMATION

Supplementary information The online version contains supplementary material available at https://doi.org/10.1038/s41535-022-00465-3.

Correspondence and requests for materials should be addressed to Zheng Yan, Yan Chen or Xue-Feng Zhang.

Reprints and permission information is available at http://www.nature.com/reprints

Publisher's note Springer Nature remains neutral with regard to jurisdictional claims in published maps and institutional affiliations.